Proton exchange membrane-like alkaline water electrolysis using flow-engineered three-dimensional electrodes

Fernando Rocha[1], Christos Georgiadis [1], Kevin Van Droogenbroek[1], Renaud Delmelle [1], Xavier Pinon[1], Grzegorz Pyka [1], Greet Kerckhofs [1], Franz Egert [2,3], Fatemeh Razmjooei [2], Syed-Asif Ansar[2], Shigenori Mitsushima[4] & Joris Proost[1] ✉

For high rate water electrolysers, minimising Ohmic losses through efficient gas bubble evacuation away from the active electrode is as important as minimising activation losses by improving the electrode's electrocatalytic properties. In this work, by a combined experimental and computational fluid dynamics (CFD) approach, we identify the topological parameters of flow-engineered 3-D electrodes that direct their performance towards enhanced bubble evacuation. In particular, we show that integrating Ni-based foam electrodes into a laterally-graded bi-layer zero-gap cell configuration allows for alkaline water electrolysis to become Proton Exchange Membrane (PEM)-like, even when keeping a state-of-the-art Zirfon diaphragm. Detailed CFD simulations, explicitly taking into account the entire 3-D electrode and cell topology, show that under a forced uniform upstream electrolyte flow, such a graded structure induces a high lateral velocity component in the direction normal to and away from the diaphragm. This work is therefore an invitation to start considering PEM-like cell designs for alkaline water electrolysis as well, in particular the use of square or rectangular electrodes in flow-through type electrochemical cells.

The increasingly extreme effects of anthropogenic climate interference necessitate urgent actions to limit the rise in global average temperature[1]. To address these threats, the international community has united for more than 3 decades under several climate agreements[2–4] trying to impose a transition from fossil fuels to renewable energy sources[5]. While electricity is projected to become the primary energy carrier in a net-zero society, there are energy needs for which electricity cannot easily or economically replace fossil fuels[6]. In this context, hydrogen and hydrogen-based fuels emerge as promising alternatives to meet specific needs[6]. Hydrogen exhibits remarkable flexibility, as it can be converted to electricity through fuel cells[7] or gas turbines[8], and to

heat through burners[9]. Moreover, hydrogen can be converted to other fuels, such as ammonia through the Haber-Bosch process[10] or synthetic kerosene through Fischer-Tropsch reactions[11]. As a result, hydrogen and hydrogen-based fuels are expected to play a crucial role in transport to power long-haul heavy-duty trucks[6], ships[12] and airplanes[6]. Additionally, since most renewable energy sources generate energy intermittently, hydrogen also offers a solution for long-term energy storage and load balancing[13,14]. Furthermore, hydrogen can contribute as well to the decarbonization of industrial sectors, like replacing coal as a reducing agent in steel factories[15] or substituting fossil fuels in the provision of high-temperature heat as in the cement industry[6].

[1]Division of Materials and Process Engineering, Université catholique de Louvain, Louvain-la-Neuve, Belgium. [2]Institute of Engineering Thermodynamics, German Aerospace Center, Stuttgart, Germany. [3]University of Stuttgart, Faculty 6 - Aerospace Engineering and Geodesy, Stuttgart, Germany. [4]Division of Materials and Chemical Engineering, Yokohama National University, Yokohama, Japan. ✉e-mail: joris.proost@uclouvain.be

Water electrolysis driven by renewable electricity stands as the most sustainable approach to hydrogen production[16]. At present, there are two commercially available technologies: alkaline and proton exchange membrane (PEM)[17]. The former presents the lowest capital cost per kilowatt of electricity[18] but suffers from the lowest hydrogen production rate per electrode area[19]. PEM electrolysis can achieve much higher production rates, but depends on scarce and expensive electrocatalytic materials, such as iridium and platinum[19]. The ideal electrolyser should combine the advantages of both systems, presenting high production rates while using inexpensive and abundant electrode materials[20].

In this respect, the major novelty of the current work is that we have been able to demonstrate that for water electrolysis, efforts in tailoring the electrode's topology towards enhanced bubble evacuation has the potential of a similar performance improvement than when merely optimising its electro-catalytic composition. This opens up a new and yet largely unexplored degree of freedom in the design of highly performing electrodes for use in next generation high-rate electrolysers. Since these are made to operate at ever increasing current densities (>1.0 A·cm⁻²), bubble removal efficiency (mass transfer) can be expected to become as important as the electrochemical reaction itself (electron transfer). In particular, by a combined experimental and computational fluid dynamics (CFD) approach, we have identified the electrode's 3-D structural parameters that allow to tune its performance towards enhanced bubble evacuation. We also demonstrated that integrating such flow-engineered 3-D electrodes into a laterally-graded cell configuration allows to significantly boost the performance of alkaline water electrolysis up to 2 A·cm⁻² at <2 V cell voltage, even when keeping a state-of-the-art Zirfon diaphragm. The improved performance was shown to be the synergistic effect of 3 factors, as illustrated in Fig. 1: (1) the use of a forced high upstream electrolyte flow in a dedicated zero-gap flow-through cell, as opposed to the serpentine flow fields often used in the literature; (2) the integration of 3-D electrodes using a bi-layer configuration consisting of a fine and thin foam in contact with a coarse and thick foam, the combination being flow-engineered to enhance gas removal; (3) the application of a Ni-based coating on the fine foam and its activation into Raney Ni in both the anodic and cathodic parts, resulting in catalytically highly active electrodes free of Pt group metals that are able to maintain their activity at high current densities thanks to the improved bubble evacuation.

We are aware that quite a bit of prior art, both in PEM fuel cells and electrolysers, already reported on the use of so-called 3-D porous electrodes, including foams and meshes[21–23]. However, in most of these configurations, these were rather used as porous transport layers (PTL) only allowing for and not necessarily enhancing bubble evacuation. Such PTL are then typically used in combination with electrocatalytic elements like perforated plates. However, the latter rather serve as 2-D electrodes, not as 3-D porous electrodes, in the sense that no upstream electrolyte flow can pass *through* these electrodes. In this work, we report on the use of a flow-through bi-layer 3-D foam configuration and demonstrate how such a configuration induces particular electrolyte flow characteristics thanks to a pressure gradient in the direction normal to and away from the diaphragm that allow to enhance bubble removal.

Results and discussion
PEM-like alkaline water electrolysis using a state-of-the-art Zirfon diaphragm
The synergy demonstrated in this work by the use of 3-D electrodes in a flow-engineered bi-layer zero-gap cell geometry can be best understood and appreciated when comparing to available literature data. Several recent papers on alkaline water electrolysis under similar conditions (temperature 70−80 °C, KOH concentration 24−30 wt%) and using a Zirfon gas separator and Ni-based electrode materials are summarised in Table 1. Note that a state-of-the-art Zirfon diaphragm was chosen in this work in order to have the largest possible consistent comparative data set from the literature. A further performance improvement can be expected using our same 3-D electrode and cell configuration but replacing the Zirfon diaphragm with more conductive alkaline-based membranes[19,24].

Representative polarisation curves are shown in Fig. 2 for two upstream flow velocities for a pure Ni bi-layer (a) and a bi-layer with a catalytic Raney Ni coating (b). The available literature range is indicated as well. In order to gain more insight into the significant performance enhancement that was obtained in both cases, all polarisation curves within the literature range, which are shown in full detail in Supplementary Fig. S1, have been fit using the following fundamental equation[25]:

$$E_{cell} = E_{eq} + b \cdot \log\left(\frac{j}{j_0}\right) + R_{total} \cdot j \qquad (1)$$

with E_{cell} the measured cell voltage, E_{eq} the equilibrium cell voltage, and j the imposed current density. The free fitting parameters in the above equation are b, i.e. the sum of the Tafel slopes for the cathodic and anodic reaction, the non-linear average j_O of their respective exchange current densities, and the total Ohmic resistance R_{total}. The latter consists of the resistance of the Zirfon diaphragm and any remaining electrolyte resistance, potentially influenced by non-evacuated bubbles, that is not shunted by the zero-gap configuration. As illustrated in Supplementary Fig. S1, R_{Zirfon} can then be subtracted out based on known data from the literature, thereby revealing the specific contribution of non-evacuated bubbles as $R_{total} - R_{Zirfon}$.

All fitting results, including standard deviations, have been summarised in Supplementary Table S1, and are shown as cumulative normal distributions in Fig. 3 for the Tafel slope b (top) and $R_{total} - R_{Zirfon}$ (bottom), respectively. For more details on the interpretation of such a data representation in the form of a cumulative normal distribution, we refer to Supplementary Fig. S3 in SI. Two important observations can be made from these graphs. First of all, the use of a catalytic Raney Ni coating results in a significant decrease in Tafel slope, and hence an improved electrochemical performance, as is already well-documented in the literature. However, fitting results for our own polarisation curves do not differ markedly from literature data: the b-values for both our pure Ni and Raney Ni bi-layers fall on the same cumulative normal distribution as the respective literature data. Therefore, our observed performance enhancement cannot be ascribed to the use of Raney Ni alone.

Secondly, the Zirfon-corrected part of the Ohmic resistance ($R_{total} - R_{Zirfon}$) for the polarisation curves obtained in this work clearly do fall on a different cumulative normal distribution, and the obtained values are also significantly lower than previously reported literature values. This indicates that, although applying a Raney Ni coating is a necessary contribution to the reported performance enhancement, it is the lowering of the contribution of non-evacuated bubbles to the Ohmic resistance in a zero-gap cell configuration that allows to make the difference. This is explicitly confirmed by the fact that, from Supplementary Table S1 and Fig. 3b, no significant difference in Ohmic resistance was observed after coating: the value of $R_{tot} - R_{Zirfon}$ at 0.35 l·min⁻¹ and 1.60 l·min⁻¹ was 152.3 ± 0.7 mΩ·cm² and 130.4 ± 0.5 mΩ·cm², respectively for our pure Ni foams, and 145.9 ± 0.3 mΩ·cm² and 128.4 ± 0.2 mΩ·cm², respectively for our Raney Ni foams. We will show below through detailed CFD simulations that it is rather the use of a flow-engineered bi-layer configuration, combined with applying a forced upstream electrolyte flow that allows for the enhanced bubble evacuation.

Finally, we are well aware that Anion Exchange Membrane Water Electrolysis (AEMWE) has already been shown to provide current densities easily surpassing 2 A·cm⁻² at 2 V cell voltage[26]. However, the
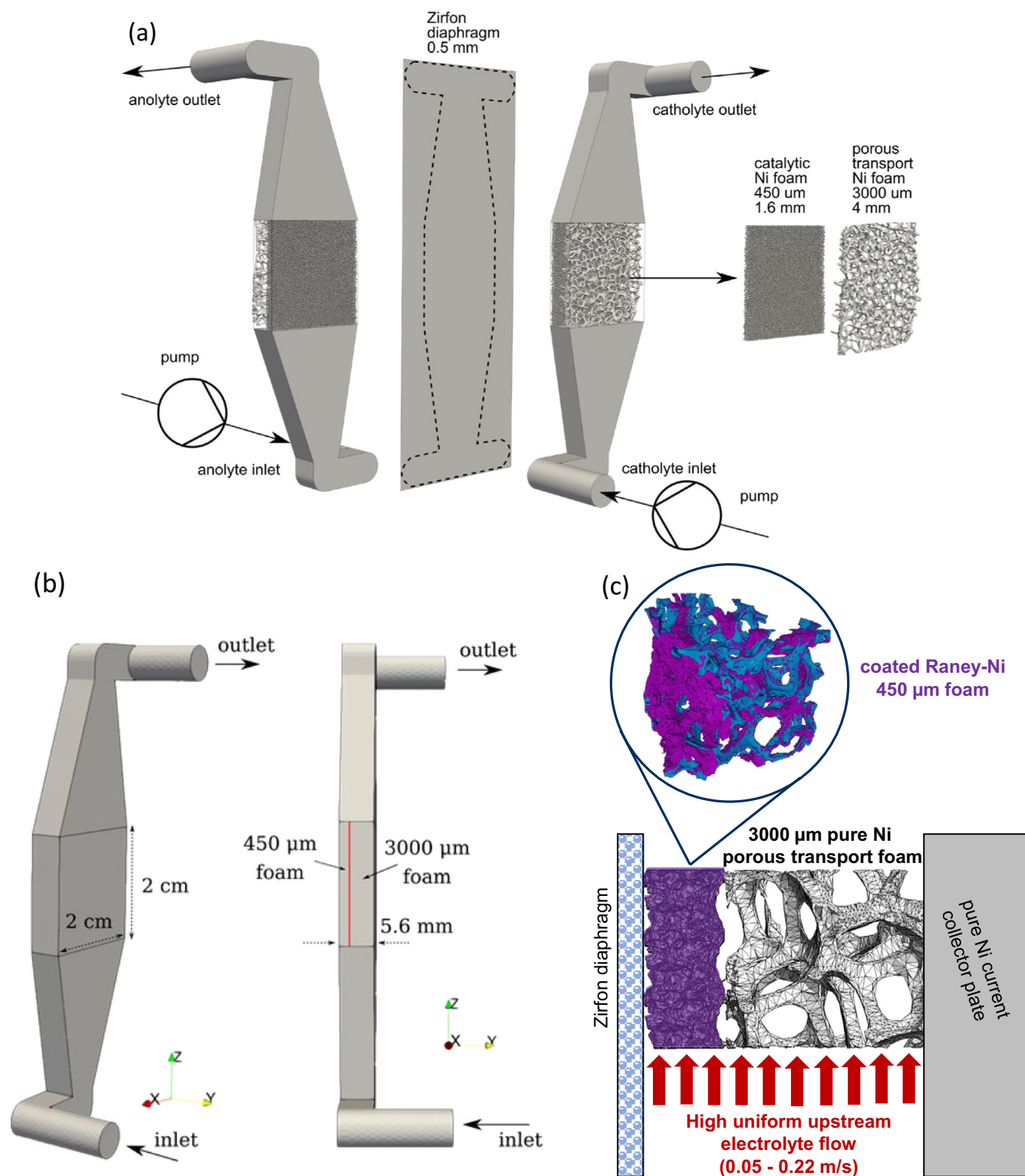
Fig. 1 | Details of the structure and arrangement of our dedicated zero-gap flow-through cell, using a high uniform forced upstream electrolyte flow. **a** Flow and pumping direction of both anolyte and catholyte and the position of the bi-layer foam electrodes. The area of the rectangular 4.5 × 9.5 cm² Zirfon diaphragm exposed to the electrolyte is enclosed by dashed lines. It is larger than the fluid domain (2 cm width) to prevent leakage; **b** integration of 3-D electrodes using a bi-layer configuration consisting of a fine, 1.6 mm thin 450 μm pore size foam in

contact with a coarse, 4 mm thick 3000 μm pore size foam as porous transport layer, the combination being flow-engineered to enhance gas removal; **c** application of a Ni-based coating on the fine foam and its activation into Raney Ni in both the anodic and cathodic parts, resulting in catalytically highly active electrodes free of Pt group metals. The coating exposed surface is facing the 500 μm thick Zirfon diaphragm.

Table. 1 | Details of cell setups reported in the literature for alkaline water electrolysis with a Zirfon separator and PGM free electrodes

Ref.	KOH (wt.%)	Temp. (°C)	Cathode	Anode	Flow (ml·min⁻¹)	Electrode area (cm²)	Transport/contact layer
This work	30%	70	Ni 450 μm foam	Ni 450 μm foam	350–1600	4	3000 μm Ni foam
This work	30%	70	Raney-Ni 450 μm foam	Raney-Ni 450 μm foam	350–1600	4	3000 μm Ni foam
32	30%	80	Raney Ni perforated plates	Raney Ni perforated plates	50	25	Flow field (shape N/S)
70	5%ᵃ	80	Stainless steel expanded mesh	Stainless steel expanded mesh	80	10	Serpentine flow field
31	30%	80ᵇ	Ni plate with channels	Ni plate with channels	0.048–288	19.63	Flow field (shape N/S)
19	24%	80	Ni foam	Ni perforated sheet	50	25	Flow field (shape N/S)
19	24%	80	Raney Ni perforated sheet	Raney Ni perforated sheet	50	25	Flow field (shape N/S)
33,34	30%	80	Ni foam	Ni foam	450	34.56	Serpentine flow field
33,34	30%	80	Raney Ni foam	NiFe-LDH foam	450	34.56	Serpentine flow field
61	26% (6 M)	70	Raney Ni multimesh	Raney Ni multimesh	Unknown	4	Knitted Ni wire
71	N/S	80	Ni foam	Ni foam	100	5	Serpentine flow field
72	30%	80	Raney Ni foam	NiFe-LDH foam	400	36	Ni foam
73	30%	80	Porous Raney Ni	Porous NiFe-LDH	400	25	Serpentine flow field
24	26% (6 M)	80	Ni foam	Ni foam	50	4	Serpentine flow field
74	30%	80	Raney nickel foam	NiFe-LDH foam	1000	34.56	Porous transport layer

N/S not specified
ᵃNaOH as electrolyte
ᵇ30 bar of pressure

main novelty of the current paper is that the integration of well-known electrocatalysts (Raney Ni) and a state-of-the-art durable gas separator (Zirfon diaphragm) into a well-thought flow-engineered cell design based on a laterally-graded bi-layer 3-D foam configuration has the potential to significantly boost the performance of standard alkaline water electrolysers towards PEM-like behaviour (even without the need for new catalyst or membranes). Raney Ni electrodes and a Zirfon diaphragm were simply considered in this paper as well-known benchmark components, allowing to demonstrate and isolate the effect of the flow-engineered bi-layer cell design.

Forced uniform upstream electrolyte flow

From Fig. 2 and Supplementary Table S1, it can be seen that an increase in electrolyte flow rate from the minimum to the maximum value (i.e. from 0.35 to 1.6 l·min⁻¹) caused a decrease of $12.0 \pm 0.2\%$ and $14.4 \pm 0.5\%$ in Ohmic resistance for the coated and the non-coated foam, respectively. The observed effect is attributed to enhanced bubble removal caused by the forced upstream electrolyte flow. Before the start of hydrogen and oxygen production, both the electrode surface and the electrolyte are free of bubbles. As soon as gas evolution starts, bubbles start to nucleate and grow on the electrode surface and pass into the electrolyte once a critical size is achieved. Any adhering insulating bubbles decrease the electrochemically active electrode surface (screening effect)[27], while detached bubbles tend to lower the electrolyte conductivity (voidage effect)[28]. An increase in upstream flow rate (i.e. in the direction of gas evacuation) is capable of shortening the bubble growth time and decrease its maximum size, thereby lowering the voltage loss in traditional gap-cells[29]. In the case of a zero-gap cell configuration however, Haverkort[30] convincingly showed that any effect of non-evacuated bubbles on the Ohmic resistance is restricted to electrolyte areas that are not shunted by the much more conductive 3-D electrodes. This may include their trapping inside the micro-porous Zirfon diaphragm or in the small gap (typically 50–100 μm thick[25]) that usually remains between the Zirfon and the electrode area facing the diaphragm (see also Fig. 1c). In particular, ref. 30 demonstrated, both theoretically and experimentally, that the frontal area of expanded metal electrodes, i.e. the area facing the diaphragm, was not electrically active in a zero-gap cell using a Zirfon separator. This was attributed to the fact that gas bubbles either enter the separator or block the electrode surface in the region between the electrode and the separator, hence creating a screening effect which increases the Ohmic resistance. The fact that our $R_{tot} - R_{Zirfon}$ values are significantly lower than the literature is therefore an indication of a much better bubble removal efficiency in our flow-engineered bilayer zero-gap cell, not only in the interior of the 3-D electrode itself (which in the case of zero-gap cells is not measurable via the Ohmic resistance) but also in the small region remaining between the 3-D electrode and the separator. Also note in Fig. 2 how the polarisation curves at minimum flow show many irregularities, indicative of poor bubble evacuation, while it becomes much smoother when increasing the flow rate.

Looking first at the data for our pure Ni electrodes, their performance clearly outperforms the ones previously reported in the literature. At a constant current density of 1.8 A·cm⁻², the best result from the literature was a cell voltage of 2.6 V[24], whereas our own study achieved a significantly lower voltage of only 2.1 V. Both studies used 2×2 cm² Ni foam electrodes, but instead of using a coarse porous transport foam as we did, ref. 24 used a serpentine-like flow plate at a flow rate of only 0.05 l·min⁻¹, which is 7 times lower than the minimum flow used in our work. In terms of Zirfon corrected Ohmic resistance ($R_{total} - R_{Zirfon}$), our work achieved a minimum value of 130 ± 1 mΩ·cm² for pure Ni electrodes, which is lower than the lowest literature value of 143 ± 8 mΩ·cm², reported in ref. 31 at a pressure of 30 bar. While it is well-known that at higher pressures, the bubble size decreases thereby reducing their contribution to the overall cell voltage, our flow-engineered 3-D electrodes proved to be superior even under atmospheric conditions.

Secondly, as to the coating effect, in ref. 19 the Ohmic resistance doubled when going from pure Ni to Raney Ni, reaching 297 ± 5 mΩ·cm². This indicates that in that work, the use of serpentine-like flow plates was unable to efficiently remove the higher amount of gas bubbles produced at the Raney Ni electrodes. In ref. 32 2-D perforated coated Raney Ni plates were used as electrodes, but again in the presence of non-optimised flow fields and a low flow rate of 0.05 l·min⁻¹. As a result, their Ohmic resistance was 270 ± 4 mΩ·cm², twice as high as in our work. Refs. 33,34 compared different Raney Ni-based foams as electrodes. The electrolyte flow rate in these studies was set at 0.45 l·min⁻¹, but since the electrode area was 34.56 cm²,
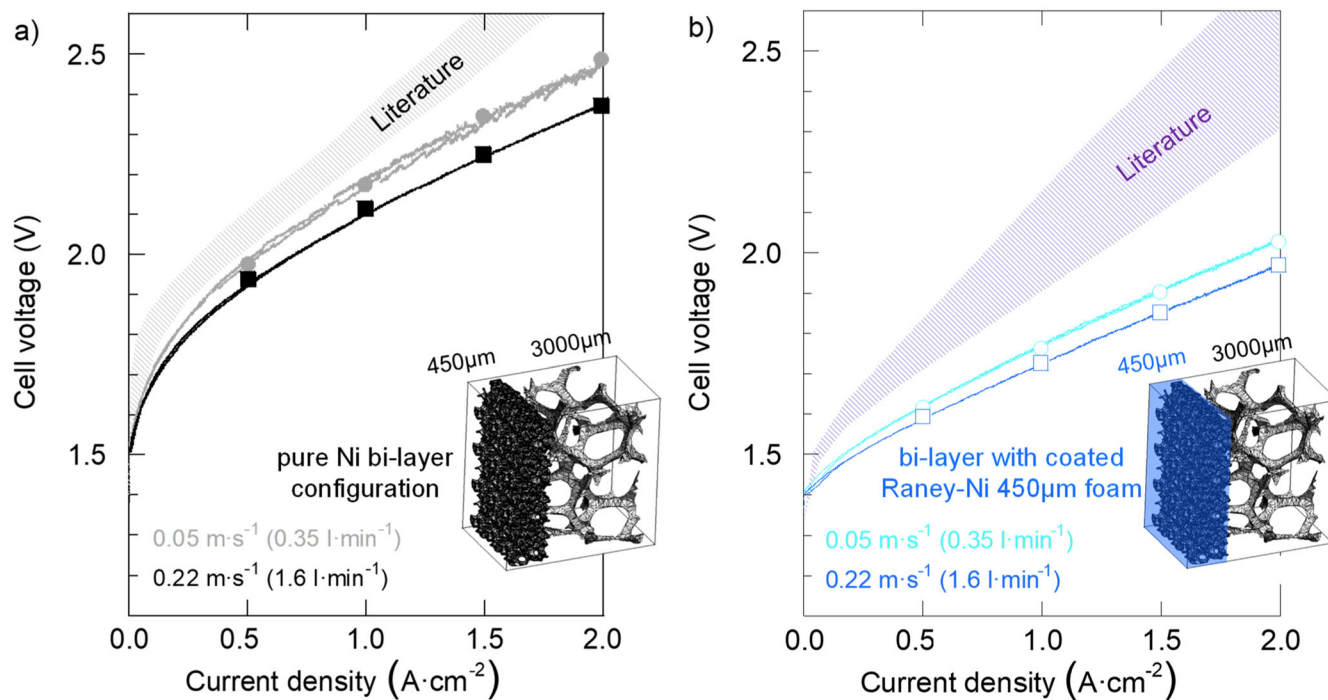
Fig. 2 | Representative polarisation curves (not iR corrected) at 70 °C and 30 wt.% KOH for 2 electrolyte upstream flow velocities. a A pure Ni 450/3000 μm bi-layer foam and **b** a bi-layer with a catalytic Raney Ni coating on the 450 μm foam. A structural representation of the bi-layer as obtained from X-ray micro-computed tomography is included within the figure. Lines are measured from cyclic voltammetry, with bullet points from galvanostatic experiments being superimposed. Hatched zones represent the range of literature data, for which all polarisation curves are shown in Supplementary Fig. S1.

almost 9 times larger than in our case, this corresponds to a mere 0.05 l·min^{-1} as well when normalised to the same electrode area of 4 cm^2. In ref. 34, the nature of the porous transport layer was not specified, but in ref. 33 a single serpentine flow field was used. The result was an Ohmic resistance of 300 ± 10 mΩ·cm^2, more than double the value we obtained by our flow-engineered bi-layer configuration under high upstream flow.

Based on the above comparison with literature data, we can already conclude that the serpentine flow fields often used in the literature are not the best way to enhance bubble removal. It seems that they have been simply adopted without further question from transport studies related to fuel cells[35,36]. However, mass transport in fuel cells involves the transport of gases as reactants away from the flow field into the catalyst layer. This is fundamentally different from the basic functioning of a water electrolyser, where the main transport issue is the evacuation of gas bubbles as the reaction product away from the electrode. Our own cell design and electrode configuration also mitigate the negative effects of high electrolyte flows, most notably the occurrence of jet-like, unstable flows due to small inlet diameters. Instead, in our dedicated flow cell, the flow is uniformly distributed over the entire width of the bi-layer electrode. This results in an enhanced transport of bubbles away from the catalytic foam, either directly to the outlet or laterally towards the coarse porous transport foam. This will be demonstrated in the next section by both single and 2-phase simulations that explicitly take into account the 3-D bi-layer electrode topology.

Serpentine flow fields rather impede such a bubble extraction. This is illustrated in Supplementary Fig. S2 by comparing its so-called Cumulative Distribution Function (CDF) and Residence Time Distribution (RTD) function to the one for our bi-layer configuration. As to the CDF (Supplementary Fig. S2e), it can be seen that the time required for the fraction of tracers to reach 100% of the exit stream is significantly lower for the flow-engineered bi-layer configuration. This already suggests that our bi-layer configuration will lead to a faster

bubble extraction as well. The latter is confirmed by the RTD functions in Supplementary Fig. S2d: the major fraction of tracers leaving the cell spend less time in our bi-layer configuration than when using the serpentine flow field, resulting in a much smaller mean residence time. Moreover, the RTD function of the bi-layer configuration also has a narrower distribution, meaning that passive scalars convected by the electrolyte flow leave the cell after having spent similar residence times. This indicates that our bi-layer configuration also favours electrolyte and bubble flow directly towards the outlet of the cell. In the case of a serpentine flow field, bubble extraction is rather impeded due to back-and-forth flow circulations at the interface between the catalytic region and the flow channels, as illustrated by the velocity streamlines in Supplementary Fig. S2c,d. This not only leads to a higher mean residence time, but also to a much broader residence time distribution.

An important remark relates to the electrochemical methodology that was used to extract the above-discussed data. It was based on fitting of polarisation curves according to electrochemical Eq. (1), a well-documented practice in the literature[25] and the only available way to consistently compare our own results to data from the literature. However, by using Eq. (1), an important assumption was made, namely that the value of the Ohmic resistance R_{tot} obtained from fitting can be considered independent of current density. If we associate this value (and therefore also the value of $R_{tot} - R_{Zirfon}$) with non-evacuated gas bubbles, it is not unlikely that it might change (increase) upon increasing current density, as a result of an increased gas production rate. Therefore, we also performed Electrochemical Impedance Spectroscopy (EIS) measurements at 2 different flow rates on our pure Ni bi-layers, and compared the obtained results for the high frequency resistance at different current densities in the range 0.01–2 A·cm^{-2} to the (single) value of R_{tot} obtained from fitting the entire polarisation curve to Eq. (1). Results are included in SI as Supplementary Fig. S4. A first important observation is that for both flow rates, the EIS-derived high frequency Ohmic resistance shows very little variation with
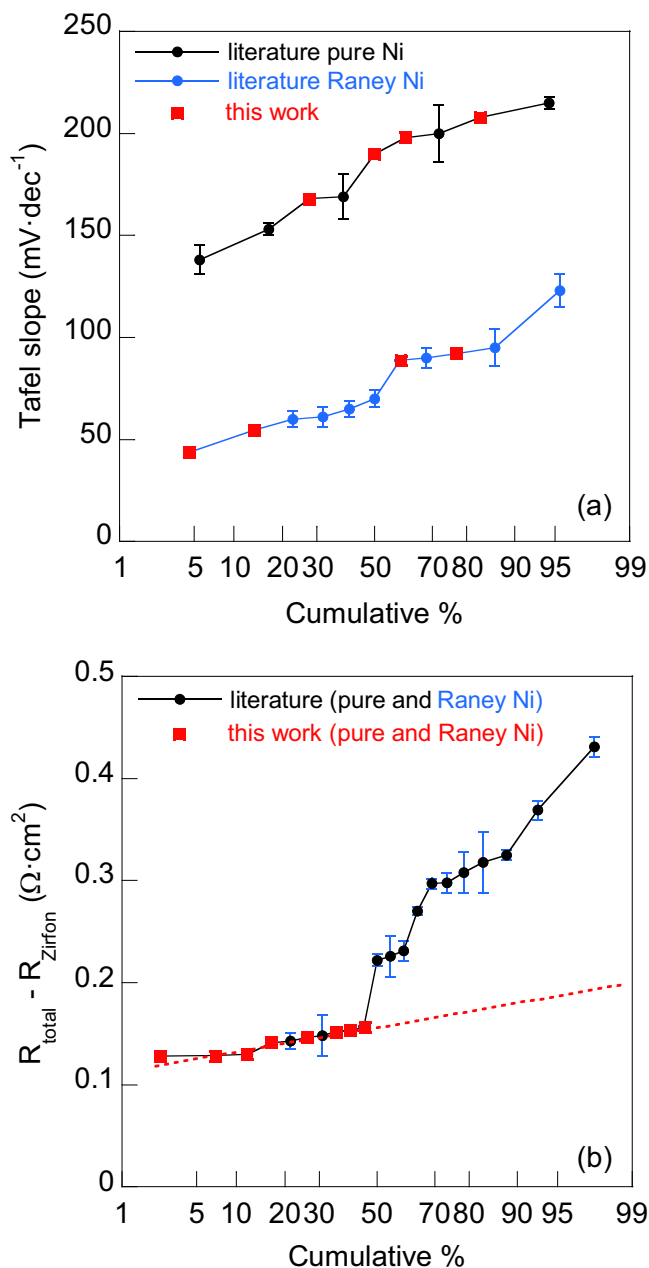
Fig. 3 | Cumulative normal probability plots comparing our own data to relevant data from the literature using Ni-based electrodes and a Zirfon diaphragm. a Tafel slopes and **b** area-specific Ohmic resistance minus Zirfon resistance. Raw data are compiled in Supplementary Table S1 and obtained by fitting all polarisation curves by Eq. (1). Data from this work are taken at 70 °C and 30 wt% KOH. Error bars represent the standard deviation on the free fitting parameters of Eq. (1). The red dotted line in (**b**) is simply a guide to the eye.

in the case of a perforated 2-D plate electrode, much smaller than our reported $R_{tot} - R_{Zirfon}$ values.

A related comment can be made on the magnitude of the error bars on the $R_{tot} - R_{Zirfon}$ data, as reported in Supplementary Table S1 and included in Fig. 3b as well. As to the latter, they are barely visible for our own data set (red symbols), simply because the relative error was always very small, much smaller than the error on the black and blue literature data. This is an important additional observation that can also be fully understood from the additional EIS measurements discussed above. Indeed, the small error on our own curve fitted Ohmic resistance data can be taken as indicative for the fact that R_{tot} shows very little variation with current density, a statement which was explicitly confirmed by EIS. Moreover, since current density is proportional to bubble production rate, a current density in-dependent value of R_{tot} can also be taken as indirect proof for the high bubble removal efficiency of our own flow-engineered cell configuration. Indeed, all bubbles generated within the catalytic foam will be driven to the PTL and evacuated out, giving the same low value of R_{tot} at low and high current density, i.e. at low and high bubble production rate.

Laterally-graded bi-layer zero-gap cell configuration
The integration of our 3-D bi-layer foam electrodes into a zero-gap cell configuration has been optimized for enhanced bubble evacuation with the help of both single-phase and 2-phase CFD simulations. Particular attention was given to the understanding of the dynamics of electrolyte flow through macro-porous 3-D electrodes. Traditionally, flow in such porous media has been simulated by averaged equations based on the Representative Elementary Volume theory[37]. Progress in computational power has now made it possible to tackle the problem by explicitly describing the full topology of the porous electrode. The latter involves the use of X-ray micro-computed tomography to obtain high-resolution scanning data of the foam topology[38–40]. Based on these scanned data, a meshing workflow was then applied as described in Supplementary Fig. S5 of the SI to obtain computationally ready meshes for our electrode foams, similarly as in refs. [41,42]. The detailed flow characteristics are then investigated, with a particular focus on the interface dynamics between a fine catalytic foam acting as a gas production layer and a coarse porous transport foam (PTF) acting as a bubble extraction layer.

In a first step, we have based our initial bi-layer configuration on the experimental results of bubble evacuation efficiency as a function of pore size that we already reported in previous work[43]. In that paper, a drastic increase in available surface fraction, indicative of enhanced bubble removal, was reported from 1000 µm pore sizes onwards. Therefore, our initial bi-layer configuration consisted of a fine, high surface 450 µm foam as a gas production layer, combined with a coarse 3000 µm porous transport foam used as a bubble extraction layer. In order to quantify the bubble extraction capability of our bi-layer configuration, we then extracted from our simulations the y-velocity component averaged over x-z planes for each position normal to the diaphragm. This scalar quantity can be taken as indicative of mass transfer in the lateral y-direction, i.e. in the direction normal to and away from the diaphragm. Figure 4 shows that already for the single-phase simulations, a clear velocity increase is observed as we move towards the coarse bubble evacuation layer, with peaks that depend on the local foam morphology. Its driving mechanism is the pressure discontinuity on the interface between both foams. Indeed, the fine 450 µm catalytic foam acting as the gas production layer exhibits a much higher flow resistance as compared to the coarse 3000 µm porous transport foam (PTF). For example, for an inlet velocity of 0.22 m·s⁻¹, the upstream z-velocity through the coarse PTF is 0.30 m·s⁻¹ while for the fine gas production layer it is only 0.06 m·s⁻¹. As a consequence, bubbles that are produced within the fine catalytic foam will be evacuated laterally into the porous transport foam, so that the high catalytically active surface area of the former no longer suffers from

imposed current density: for an electrolyte flow rate of 0.35 l·min⁻¹ and 1.2 l·min⁻¹, it ranges between 0.24 to 0.30 Ω·cm² and 0.23 and 0.27 mΩ·cm², respectively, with an average value of 0.26 ± 0.02 Ω·cm² and 0.24 ± 0.02 Ω·cm², respectively. Moreover, these average values (with a relative error in both cases of less than 10%) are also statistically equal to the polarisation curve-fitted values for R_{tot} of 0.27 Ω·cm² and 0.24 Ω·cm², respectively, already reported in Supplementary Table S1. Both of these findings give further confidence to the $R_{tot} - R_{Zirfon}$ data from our own polarisation curves as presented in Fig. 3b, and in the validity of the associated conclusions related to enhanced bubble removal. They also allow to exclude any significant contribution of current inhomogeneities, which was estimated in ref. 25 as 0.02 Ω·cm²
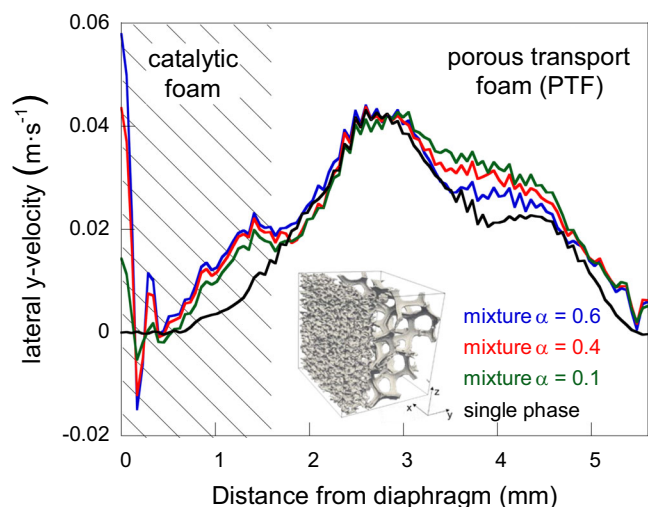
Fig. 4 | Averaged lateral velocity profiles in the direction normal to the diaphragm as a function of distance for single-phase and 2-phase simulations, the latter with different gas fractions α. The upstream electrolyte inlet velocity was set at 0.22 m·s⁻¹. The fine 450 μm pore size catalytic foam is indicated by the dashed region. The inserted picture is the structural representation of the pure Ni 450/3000 μm bi-layer foam used for the CFD simulations, as obtained from X-ray micro-computed tomography.

bubble entrapment. More details on the simulated flow-induced pressure gradients and their relation to the expected buoyancy forces have been included in SI (Supplementary Fig. S6).

The above conclusions derived from single-phase simulations are further confirmed (and even enhanced) when considering 2-phase flow, as shown in Fig. 4 as well. Our 2-phase modelling approach, which was based on a simple mixture model with hydrodynamic dispersion, was to start with a stagnant gas mixture inlet with different gas fractions α at the interface of the catalytic foam and the diaphragm (i.e. at distance y = 0 in Fig. 4) and then see the variations in the lateral velocity profiles as a function of gas fraction when moving in the direction normal to the diaphragm. Three important and interrelated observations can be made on Fig. 4 when comparing these 2-phase simulations to the single-phase ones. First of all, a significantly higher lateral velocity is obtained for the 2-phase mixtures, in particular at y = 0, i.e. at the interface of the diaphragm and the fine catalytic foam. This is also the location where in our simulations the gas fraction was localised initially. Secondly, this increase in lateral velocity is correlated with an increase in the negative direction of the lateral velocity component in the zone neighbouring the diaphragm. This is indicative for electrolyte flow being directed towards the diaphragm near its interface. Note that in the single-phase simulations, this negative lateral velocity component was present as well, but with a value of only −0.0002 m·s⁻¹, and hence barely visible on the ordinate scale of Fig. 4. Finally, the lateral velocity obtained from our simulations for 2-phase mixtures is now significantly higher over the entire thickness of the fine catalytic foam (where bubble generation is being localised) as compared to the single-phase case. In other words, bubble evacuation from the catalytic foam into the coarse PTL foam can be expected to be even more enhanced as compared to the single-phase simulations. We associate this enhanced lateral velocity of the 2-phase mixture with an increased fraction of upstreaming electrolyte being sucked into the catalytic foam, as a result of a less dense mixture situated near the diaphragm (i.e. at y = 0 in our simulations). The latter is shown more clearly in Fig. 5, which compares the velocity vectors for the single-phase and 2-phase simulations (the latter for α = 0.4). By looking in detail at the entrance section of the bi-layer region (bottom figures), we can see that for the single-phase the largest fraction of upstream

electrolyte flow deviates into the coarse 3000 μm foam, while for the 2-phase simulations a significant fraction of electrolyte also enters the fine 450 μm catalytic foam. These figures also demonstrate the importance of performing 2-phase simulations using the explicit topological description of the 3-D foam bilayer configuration. Indeed, the negative lateral velocities observed in Fig. 4 are directly associated with the local morphological details of the small pore sized catalytic foam at the entrance section of the bi-layer region.

In a second step, our simulations then revealed that the 3000 μm foam is a more suitable choice as PTF as compared to other available coarse foams, such as the 2200 μm one (see Supplementary Fig. S7a in SI). It indeed exhibits a lower resistance to the upstream flow, thus creating a higher pressure difference between the catalytic and the porous transport foam. At the same time, as compared to the use of a 450 μm foam in a gap-type cell without any rigid foam-based PTL (corresponding to the "void" case in Supplementary Fig. S7a), it offers a more rigid structure to electrically connect the electrode to the flat bipolar plate and to press the catalytic foam against the separator, thereby allowing to maintain the structural and geometrical stability of our zero-gap configuration under high upstream flow conditions. In this respect, the fact that no patterning or profiling is needed of the flat bi-polar plates to improve the electrolyte flow distribution can be seen as another major advantage of our foam-based bi-layer configuration.

We also simulated the flow behaviour for different PTF thicknesses, keeping the catalytic foam thickness fixed at 1.6 mm. Since a 3000 μm sized foam was selected as the optimal PTF, a thickness of at least 4 mm is needed in order to ensure structural stability along the lateral y-direction with at least one pore per thickness. For thicknesses larger than 4 mm, it was found that the high upstream electrolyte flow may generate vortical flow instabilities and recirculation zones in the PTF. This is revealed in Supplementary Fig. S7b by the negative lateral velocity values in the PTF near the bipolar plate, causing an unwanted electrolyte backflow towards the catalytic foam. As a result, the PTF thickness was kept at 4 mm.

Finally, at the explicit request of one of the reviewers, we also performed a number of flow sensitivity experiments comparing our optimised pure Ni bi-layer foam configuration to the use of a single 450 μm foam combined with a pure Ni knitted mesh-type spacer as PTL, as is often used in industrial-scale systems. These measurements were done under galvanostatic conditions in 30 wt.% KOH but at room temperature. The reason is that, as already described in detail in ref. 44, the cell temperature in our experimental set-up is precisely controlled by the electrolyte temperature in the two separate anolyte and catholyte reservoirs. Testing at room temperature then allows to mimimise the risk for any unexpected convective effects due to a possible difference in heat transfer between both cell compartments. It also allows to have an additional reference point at zero flow (i.e. at natural convection). In order to limit the cell voltage for these room temperature experiments to <2.5 V, the applied current density was limited to 0.5 A/cm². The raw galvanostatic data are shown in SI as Supplementary Fig. S8. A significantly better flow sensitivity can be observed for the bi-layer foam configuration, not only from its much more pronounced reduction in cell voltage, but also from the larger reduction in noise when increasing the flow rate. A quantitative analysis of these data is provided in Supplementary Fig. S9a, showing that the relative reduction in cell overpotential upon increasing the flow is twice as high for the bi-layer foam configuration. These results are also confirmed by the additional CFD simulation shown in Supplementary Fig. S9b, where the lateral velocity profile in the y-direction away from the diaphragm has been compared for both configurations. These profiles clearly indicate that replacing the 3000 μm foam by a knitted mesh-type spacer as PTL will fundamentally change the flow behaviour in the cell. Even though the latter offers a higher lateral velocity within the 450 μm foam itself, it can be seen that within the knitted mesh PTL
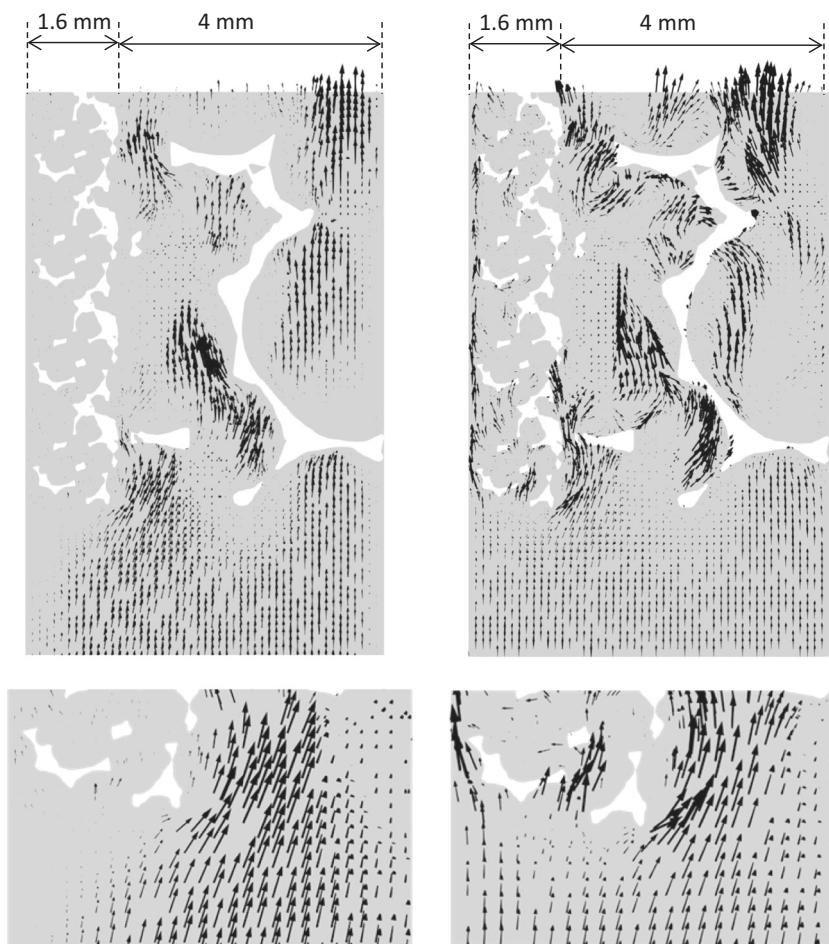
Fig. 5 | Velocity vectors scaled by magnitude for the single-phase (left) and 2-phase (right) simulations, the latter with a gas fraction of 40%. The electrolyte upstream inlet velocity was set at 0.22 m·s⁻¹, as in Fig. 4. The bottom figures are details at the entrance section of the bi-layer region. The fine catalytic foam is on the left, with a thickness of 1.6 mm. The top figures cover the entire cell width of 5.6 mm.

itself, this velocity flattens off. Therefore, the lateral y-velocity away from the diaphragm is significantly lower when considered over the entire width of the cell. This can then be expected to result in a much less pronounced bubble evacuation capacity when combining the 450 μm foam with a knitted mesh-type PTL.

Raney Ni coating and activation

As was already shown in Fig. 3a, the performance improvement by applying a thermal spray coating of Raney Ni to the fine 450 μm pore size foam was in line with existing literature data, and therefore does not represent any real novelty as such. Nonetheless, this is the first time that the application of such a Raney Ni coating and its subsequent activation has been successfully demonstrated on small pore sized foams[45]. Scanning Electron Micrographs (SEM) of both cathode and anode foams before and after coating are shown in Supplementary Fig. S9. More quantitative surface area data have been extracted as well from high-resolution X-ray tomography analysis and presented in Supplementary Fig. S10. The higher electrochemical activity of the Raney Ni bi-layer electrodes as compared to pure Ni resulted in a significantly lower Tafel slope: 49 ± 7 mV·dec⁻¹ vs. 180 ± 15 mV·dec⁻¹ for Raney Ni and pure Ni, respectively. At the same time, from Supplementary Table S1 and Fig. 3b, no significant difference in Ohmic resistance was observed after coating, resulting in similar values for $R_{tot} - R_{Zirfon}$ for our pure Ni and Raney Ni foams, respectively. This indicates that, despite its significantly increased ECSA as compared to the pure Ni foam (more than a factor 200, cfr. Methods section) and possibly different microstructural changes during operation, e.g.

related to a different formation mechanism of Ni-based (oxy) hydroxides[46,47], the Raney Ni coating does not affect the bubble evacuation capacity of our flow-engineered bi-layer zero-gap cell configuration.

We acknowledge that concerns may still exist as to the durability of the Raney Ni coating, especially when used on 3-D electrodes under forced electrolyte flow. Initial results of 500 h galvanostatic testing are shown as SI in Supplementary Fig. S11. Although the data show no performance loss over time, it should be acknowledged that they were not taken on the same dedicated flow-through cell that we used for the CV and EIS measurements. In other words, any possible degradation effect resulting from the relatively high flow rates could not be addressed in the current paper. Nonetheless, a dedicated literature review on the reliability of Raney Ni coatings was able to retrieve some encouraging long-term reliability data[48–50]. For instance, in ref. 48, Zirfon separators were evaluated in a zero-gap electrolyser using plasma-sprayed Raney Ni electrodes 250 cm² in size. During a test period of 2800 h, an excellent electrochemical stability was reported. As a more generic comment, we believe our results to remain valid as well when using any other durable catalytic 3-D electrode in a flow-through bi-layer zero-gap cell configuration, either obtained by applying a catalytic coating on a pure Ni foam, or by using a catalytically more active Ni-alloy electrode itself (like Ni-Fe or Ni-Cu). Although an optimal selection of the ultimate and most durable electrocatalyst (coating) is not the core topic of our manuscript, we can point to refs. 51–53 as a source of inspiration for any other future work.

Perspectives and strategies for future alkaline water electrolyser developments

The performance improvement for alkaline water electrolysis demonstrated in this work, with cell voltages less than 2 V at 2 A·cm^{-2}, has a number of important positive consequences for future electrolyser developments. First of all, it allows for a significant process intensification, meaning less alkaline cells are needed for a given hydrogen output. With a significantly increased power density of 2 V·2 A·cm^{-2} = 4 W·cm^{-2}, a 1 MW electrolyser would now only require 25 m^2 of electrode surface, which is 5 to 10 times less than alkaline water electrolysers producing 0.2–0.4 A·cm^{-2} at 2 V. Moreover, with today's alkaline electrodes being circular with a diameter on the order of 1 m, they typically require 160–320 cells for a 1 MW stack. Given that the more compact design allowed by our flow-engineered 3-D electrodes also allows for an easier pressurisation and sealing, and hence the use of square electrodes (as is the case for PEM), a 1 MW alkaline stack would now only require 25 cells consisting of 1 × 1 m^2 squared electrodes.

Obviously, the associated need to pump electrolyte at relatively high upstream velocities uniformly over the entire electrode surface within each cell comes at the expense of an additional energy consumption. In this respect, we had confirmation from a major industrial player that similarly high cell-level flow rates (in l·min^{-1}) are already being used in their commercial 2-stack 1 MW alkaline system. Moreover, as to the additional energy consumption required for pumping the electrolyte at such high flow rates, estimations based on confidential data from the same industrial player indicated that this would only add about 1.6 kWh·kg^{-1} per stack. This is less than 2% of the 47.9 kWh·kg^{-1} electrical energy consumed by the stack for H$_2$ production. However, there still remains a design challenge to assure that during scale-up these similar flow rates also result in similarly high and uniform superficial upstream flow velocities (in m·s^{-1}) over the entire electrode surface. In this respect, the conversion from circular to square electrodes (as is already the case for PEM) might open up new electrolyte flow design pathways in alkaline water electrolyser cells as well.

One may then also question the impact of such an increased electrolyte flow rate on the shunt current when implementing our 3-D bi-layer electrodes in an industrial-scale electrolyser stack. It represents the ionic current that passes through the electrolyte manifold, hence by-passing the cells in parallel. A most recent and comprehensive analysis of shunt currents has been reported by Sakas et al.[54], who considered an industrial 2-stack 3 MW alkaline system, each stack containing 163 cells operating in series at 1.9 V and 0.23 A·cm^{-2} in 25 wt.% KOH at 70 °C, with an electrolyte flow rate of 985 l·min^{-1} (i.e. 985/163 = 6.1 l·min^{-1} per cell). The same study also included a detailed quantitative sensitivity analysis to various process conditions, like electrolyte flow rate and supplied current. With respect to the effect of increasing electrolyte flow, this was shown to result in a significant increase in shunt current, in line with earlier literature reports[55,56]. Extrapolating the data from ref. 54 for their reference flow rate to the one that would be needed to align with the highest flow velocity of 0.22 m·s^{-1} that we used at the cell level, this would result to a 2.2-fold increase in shunt current. On the other hand, the shunt current can also be expected to decrease with the total current supply[55]. In the case of our flow-engineered 3-D electrodes, the higher electrolyte flow rate was shown to allow for a much higher current density as compared to the reference case used in ref. 54: 1.70 A·cm^{-2} at 1.9 V, instead of 0.23 A·cm^{-2}. So if the number of cells, the cell area and the cell voltage are held constant, a 7.4-fold increase in total current can be imposed. Extrapolating the data from ref. 54, one then obtains a 1.8-fold reduction in shunt current. This 1.8-fold reduction in shunt current resulting from the increased total current supply is of the same order as the 2.2-fold increase in shunt current estimated from the higher electrolyte flow rate. Even more interestingly, for the same

flow-induced increase in current density, one could also choose to keep the total current constant and rather decrease the total electrode area by decreasing the number of cells. In that case, the net effect can be expected to be an even more significant decrease in shunt current as a result of a decrease in its pathlength[55]. Since this effect is known to scale with the square root of the number of cells[57], it leads to a (7.4)$^{1/2}$ = 2.7-fold reduction in shunt current, thereby fully compensating for the projected 2.2-fold increase resulting from the higher flow rate.

The technical details included in the above-cited work of Sakas for an industrial-scale alkaline water electrolyser also allow us to come back to the issue of increased electrolyte flow. We already stated above that in our own lab-scale flow-through cell, a much higher current density was obtained: instead of 0.23 A·cm^{-2} at 1.9 V as cited in ref. 54, we arrived at 1.5 A·cm^{-2} and 1.7 A·cm^{-2} at our lowest and highest upstream electrolyte velocity of 5 and 22 cm·s^{-1}, respectively (cfr. Figure 4). So if we now decide to keep, besides the cell voltage and the total current, also the number of cells constant (rather than the cell area), a decrease in cell area of a factor 1.5/0.23 = 6.5 to 1.7/0.23 = 7.4 can be realised. Since the cells referenced in ref. 54 have a diameter of 1.6 (hence a cell area of 2.0 m^2), the use of our bi-layer electrodes would allow to reduce the cell area down to 2.0/6.5 = 0.31 m^2 or 2.0/7.4 = 0.27 m^2 at our lowest and highest upstream electrolyte velocity, respectively. In the case of square electrodes, this then corresponds to respectively 55*55 cm^2 and 52*52 cm^2. If we assume a cell thickness of 0.56 cm (as in our own cell in order to perfectly fit the bi-layer foams), the industrially imposed electrolyte flow rate of 6.1 l·min^{-1} per cell would then correspond to 6100/(60*55*0.56) = 3.3 cm·s^{-1}, not so far from the lowest velocity of 5 cm·s^{-1} that we used in our own flow-through cell. To increase this upstream flow velocity even further in the industrial system, one could also consider the use of rectangular electrodes that are larger in height than in width. For instance, to arrive at the same upstream value of 5 cm·s^{-1}, this would only require a 36*84 cm^2 rectangular electrode, without the need to increase the cell-level electrolyte flow rate of 985/163 = 6.1 l·min^{-1} that is already being used in industry today. As a matter of fact, the use of similarly sized 0.30 m^2 square or rectangular electrodes in flow-through type cells is already quite common in other electrochemical engineering applications, as extensively reviewed in refs. 58,59.

Finally, from an economical point of view, the contribution of our Ni-based bi-layer foam electrodes to the estimated cost per kW of hydrogen produced is the lowest among any other electrolyser technology. This is illustrated in Supplementary Fig. S12 of the SI, where polarisation curves for different water electrolysis technologies expressing cell voltage as a function of current density (in A·cm^{-2}) have been re-considered by dividing the latter by the electrode cost (in €·m^{-2}). This then allows to express the cell voltage as a function of current per € invested. On such plots, PEM electrolysers clearly come out to be the worst as a result of the use of expensive and scarce catalyst like Pt and Ir, resulting in an electrode cost up to 15,000 €·m^{-2}. Interestingly, both our pure Ni and Raney Ni foam-based bi-layers, with electrode costs estimated at about 400 and 1000 €·m^{-2}, respectively, economically outperform any other electrolyser technology. Their low electrode cost is not only related to the use of Ni as electrode material, but also to the high porosity (>90%) and associated decrease in electrode material mass that is needed when implemented as macroporous 3-D foams.

In conclusion, we have shown that for next generation high rate alkaline water electrolysers, minimising Ohmic losses through efficient gas bubble evacuation away from the active electrode can become as important as minimising activation losses by improving the electrocatalytic performance of the electrode itself. In particular, by a combined experimental and computational fluid dynamics (CFD) modelling approach, we demonstrated that integrating flow-engineered 3-D Ni-based bi-layer foam electrodes into a laterally-

graded zero-gap cell configuration allows the electrochemical performance of alkaline water electrolysis to become PEM-like (2 A·cm^{-2} at <2 V cell voltage), even when keeping a state-of-the-art Zirfon diaphragm. Under uniform high upstream electrolyte flow conditions in the range 5–22 cm·s^{-1}, such a graded structure was shown to induce a high lateral velocity component in the direction normal to and away from the diaphragm. As a result, gas bubbles, once formed on the electrode surface, are evacuated much more efficiently, so that the electrode surface can maintain its high electrochemical activity even at high current densities. Such a performance improvement allows for a significant process intensification: a 1 MW stack would now only require 25 m^2 of electrode surface, which is 5–10 times less than what is needed in current alkaline water electrolysers. Moreover, the contribution of our Ni-based flow-engineered 3-D electrodes to the estimated cost per kW of hydrogen produced is the lowest among any other electrolyser technology. The PEM-like performance demonstrated in this work is therefore an invitation to start considering PEM-like cell designs for alkaline water electrolysers as well, in particular the use of squared or rectangular electrodes in flow-through type electrochemical cells.

Methods

Electrode preparation

The 3-D electrodes were prepared by cutting 2×2 cm^2 of a pure Ni foam (from Alantum) with a characteristic pore size of 450 μm and 3000 μm, having a thickness of 1.6 mm and 4 mm, respectively. Their electrochemically active surface area (ECSA) was already determined in a previous publication as 42.4 ± 0.5 cm^2·cm^{-3} and 9.9 ± 0.1 cm^2·cm^{-3} [43], leading to a total active surface area in our cell of 27.1 and 15.8 cm^2 for the 450 μm and 3000 μm foam, respectively. The fine foam was then coated using the same thermal process already reported elsewhere[60]. The initial coating composition before activation was (Ni-57, Al-43) and (Ni-41, Al-41, Mo-18) for anode and cathode respectively, Mo being added to the cathode to improve the kinetics of the hydrogen evolution reaction[61,62]. Activation was carried out by separately immersing the electrodes into a solution of 30 wt% KOH (>85%, VWR chemicals) and 10 wt% potassium-sodium-tartrate-tetrahydrate (>99%, Carl Roth GmbH) at 80 °C during 24 h. During this process, Al and Mo are leached out (see Supplementary Table S2) and what remains is a micro-porous Ni skeleton with a high surface area. More details on the kinetics of the activation process can be found in Supplementary Fig. S13. ECSA measurements on our Raney Ni coated and activated 450 μm foam, according to the same procedure already described in ref. 43, resulted in a value of 9000 ± 200 cm^2·cm^{-3}. Since this is more than 200 times higher than for the 450 μm pure Ni foam, the contribution of the 3000 μm pure Ni foam to the total ECSA of our Raney Ni bi-layer almost completely vanishes, being a mere 0.3%.

Electrochemical testing

The electrolyte was prepared by dissolving 30 wt% of potassium hydroxide pellets (>85%, VWR chemicals) in deionized water (18.2 MΩ·cm, Sartorius Arium 611), and always used within a few hours after preparation. The cell was prepared by stacking the following components: two end plates with fittings for the inlet and outlet of the anolyte and catholyte, respectively; two flat 2 mm thick pure Ni end-plates (>99.5%, Alfa Aesar) without any profiling or structuring as current collectors; two 4 mm thick polytetrafluoroethylene electrode housings; and a 500 μm thick Zirfon Perl UTP 500 diaphragm (from Agfa). An ethylene propylene diene monomer layer was inserted between each of these parts, and the cell was pressed using six screws with a torque of 3 N·m each to ensure sealing. Two gear pumps (GJ-N25.FF3S.A, Micropump) were used to control the catholyte and anolyte flow independently, the flow itself being monitored by flow transmitters (Honsberg, model LABO-MID1-I/U/F/C). In our setup, the electrolyte was heated at the reservoir level (made of 316 l stainless steel). As a consequence, a minimum level of electrolyte

flow is needed to maintain the temperature in the cell at 70 °C. The minimum and maximum electrolyte flow rate was 0.35 l·min^{-1} and 1.6 l·min^{-1}, respectively, corresponding in our flow-through zero-gap cell to an upstream electrolyte velocity of 0.05 m·s^{-1} and 0.22 m·s^{-1}, respectively. The electrochemical measurement protocol started with three current scans from 0 to 8 A (0 to 2 A·cm^{-2}) at 0.1 A·s^{-1}, using a Solartron Modulab XM potentiostat equipped with a 20 A booster. These were followed by 5 min of galvanostatic testing at 0.5, 1.0, 1.5, and 2.0 A·cm^{-2}, respectively, and then by three final consecutive current scans from 0 to 8 A (0 to 2 A·cm^{-2}). There can be a difference between the measured performance during current scans and galvanostatic measurements, as the first is transient and the second steady[63]. Consequently, we verified that both curves superimposed, justifying the use of the data from current scans. More details about the experimental procedure are discussed in Supplementary Fig. S14 of the supplementary information. Galvanostatic electrochemical impedance spectroscopy (EIS) measurements were performed as well in order to have an independent determination of the high frequency Ohmic resistance. The frequency range was set between 10,000 and 0.1 Hz with 3 points per decade for current densities up to 500 mA·cm^{-2}, and between 2500 and 0.1 Hz with 3 points per decade for current densities above 500 mA·cm^{-2}. The AC amplitude was 10% of the DC.

Electrode structural characterization

Both foam electrode samples (450 μm and 3000 μm) were imaged with X-ray micro-computed tomography (μCT), using a Phoenix Nanotom M (GE Measurement and Control Solutions, Germany) equipped with a 180 kV/15 W energy nanofocus X-ray tube and a diamond-coated tungsten target. The acquisition and reconstruction parameters are listed in Supplementary Table S3. All μCT datasets were reconstructed with the Datos|x software (GE Measurement and Control Solutions, Germany) and exported as XY slices (.tiff). Besides micro-computed tomography, scanning electron micrographs of the foams before and after coating were taken as well.

Computational fluid dynamics (CFD) simulations

After X-ray micro-computed tomography scanning, an initial surface model of our foam samples was then created through the scanned images. The resulting triangulated surface is not suited for numerical simulations, as it has geometrical inconsistencies as well as having a highly detailed resolution, due to the topological complexity of the model and the inherent difficulties arising in the treatment of arbitrary 3-D surfaces. As further detailed in Supplementary Fig. S5 of the SI, surface reconstruction is performed with a variation of the alpha shape algorithm[64] on the tetrahedral mesh obtained by the point cloud of the initial surface, using custom-made software based on Gmsh[65]. The final volume mesh is created with the snappyHexMesh utility of Open-FOAM. Due to restrictions on the computational size (especially for the fine 450 μm foam), we choose to mesh a representative domain of the electrode with a size of $6 \times 6 \times 5.6$ mm^3. The thickness of the gas production and porous transport foam was kept at 1.6 mm and 4 mm, respectively. In a first stage, a single-phase model was used to simulate the electrolyte flow within the bi-layer electrodes, using the pimple-Foam solver to solve the incompressible Navier-Stokes equations within the computational domain, based on the Finite Volume Method implemented in OpenFOAM[66]. Then, in order to simulate 2-phase flow, a mixture model formulation was used and implemented on the driftFluxFoam solver available in OpenFOAM. This solver solves the continuity and momentum equations for the gas-liquid mixture by weight-averaging velocity, density and viscosity as a function of the gas fraction α and the properties of each phase. In the simulations, a stagnant gas mixture inlet (considering different values of α) was imposed at the interface of the catalytic foam and the diaphragm, with zero drift velocity. In both single and 2-phase simulations, the upstream inlet velocity was fixed to 0.22 m·s^{-1}, and the kinematic

viscosity was set at $8.28 \cdot 10^{-7}$ m²·s⁻¹ for 30 wt.% KOH at 70 °C[67]. For the 2-phase simulations, the density of hydrogen was set to 0.08 kg·m⁻³ and the dynamic viscosity to $0.88 \cdot 10^{-5}$ Pa·s.

Polarisation curve fitting

In Eq. (1) used to fit all polarisation curves, the reversible cell voltage E_{eq} was estimated as[68]:

$$E_{eq} = E_{eq}^{\circ} + \frac{R \cdot T}{z \cdot F} \cdot \ln\left[\frac{(P - P_w)^{1.5}}{P_{H_2}^{\circ} \cdot \left(P_{O_2}^{\circ}\right)^{0.5}}\right] + \frac{R \cdot T}{z \cdot F} \cdot \ln\left[\frac{P_w^*}{P_w^{*\circ}} \cdot \frac{P_w^{\circ}}{P_w}\right] \quad (2)$$

with T the temperature in Kelvin, R the universal gas constant (8.3145 J·K⁻¹·mol⁻¹), F the Faraday constant (96,485 s·A·mol⁻¹), P the total pressure in bar (assumed to be equal to the atmospheric pressure, 1.01325 bar), P_w the vapour pressure of the electrolyte in bar, P_w^* the vapour pressure of pure water in bar, and z is the number of electrons exchanged during the reaction (=2). The partial and vapour pressures under standard conditions $P_{H_2}^{\circ}$, $P_{O_2}^{\circ}$, P_w° and $P_w^{*\circ}$ are equal to 1 bar. The standard equilibrium cell voltage was estimated as a function of temperature by the following expression[68]:

$$E_{eq}^{\circ} = 1.5184 - 1.54121 \cdot 10^{-3} \cdot T + 9.523 \cdot 10^{-5} \cdot T \cdot \ln(T) \\ + 9.84 \cdot 10^{-8} \cdot T^2 \quad (3)$$

with the temperature in Kelvin. The vapour pressures of water were estimated using the following expressions[68]:

$$\ln P_w^* = 37.04 - 6276 \cdot T^{-1} - 3.416 \cdot \ln(T) \quad (4)$$

$$\ln P_w = 0.01621 - 0.1380 \cdot m + 0.1933 \cdot m^{0.5} + 1.024 \cdot \ln P_w^* \quad (5)$$

with m the molality in mol·kg⁻¹.

The Zirfon resistivity was estimated as[25]:

$$\rho_{Zirfon} = \rho_s \cdot N_m \quad (6)$$

where ρ_s is the electrolyte resistivity in Ω·cm and N_m the dimensionless MacMullin number set at 2.82 as proposed in ref. 25. The electrolyte resistivity was estimated according to[69]:

$$\rho_s^{-1} = -2.041 \cdot M - 0.0028 \cdot M^2 + 5.332 \cdot 10^{-3} \cdot M \cdot T \\ + 207.2 \cdot M \cdot T^{-1} + 0.001043 \cdot M^3 - 3 \cdot 10^{-7} \cdot M^2 \cdot T^2 \quad (7)$$

with M the molarity in mol·l⁻¹.

Finally, the area resistance of the Zirfon diaphragm R_{Zirfon}, expressed in Ω·cm², can be obtained by multiplying the Zirfon Ohmic resistivity by the thickness of the diaphragm (i.e. 0.05 cm).

Data availability

The data that support the findings of this study are available at http://hdl.handle.net/2078.1/285920. Source data are provided with this paper.

References

1. O'Neill, B. C. et al. IPCC reasons for concern regarding climate change risks. *Nat. Clim. Chang* **7**, 28–37 (2017).
2. United Nations Framework Convention on Climate Change, May 9, 1992, S. Treaty Doc. No. 102–38 (1992).
3. Kyoto Protocol to the United Nations Framework Convention on Climate Change, Dec. 10, 1997, 2303 U.N.T.S. 162 (1997).
4. Paris Agreement to the United Nations Framework Convention on Climate Change, Dec. 12, 2015, T.I.A.S. No. 16–1104 (2015).
5. IPCC. *Climate Change: Mitigation of Climate Change*. Contribution of Working Group III to the Sixth Assessment Report of the Intergovernmental Panel on Climate Change (IPCC, 2022.
6. IEA. *Net Zero by 2050* (IEA, 2021).
7. Steilen, M. & Jörissen, L. Chapter 10 - Hydrogen Conversion into Electricity and Thermal Energy by Fuel Cells: Use of H2-Systems and Batteries. In *Garche JBT-EES for RS and GB,* (ed. Moseley, P.T.) 143–158 (Elsevier; 2015).
8. Öberg, S., Odenberger, M. & Johnsson, F. Exploring the competitiveness of hydrogen-fueled gas turbines in future energy systems. *Int J. Hydrog. Energy* **47**, 624–644 (2022).
9. Marocco, P., Gandiglio, M., Audisio, D. & Santarelli, M. Assessment of the role of hydrogen to produce high-temperature heat in the steel industry. *J. Clean. Prod.* **388**, 135969 (2023).
10. Nemmour, A., Inayat, A., Janajreh, I. & Ghenai, C. Green hydrogen-based E-fuels (E-methane, E-methanol, E-ammonia) to support clean energy transition: A literature review. *Int. J. Hydrogen Energy*, **48**, 29011–29033 (2023).
11. Colelli, L., Segneri, V., Bassano, C. & Vilardi, G. E-fuels, technical and economic analysis of the production of synthetic kerosene precursor as sustainable aviation fuel. *Energy Convers. Manag* **288**, 117165 (2023).
12. Inal, O. B., Zincir, B. & Deniz, C. Investigation on the decarbonization of shipping: An approach to hydrogen and ammonia. *Int J. Hydrog. Energy* **47**, 19888–19900 (2022).
13. Dawood, F., Anda, M. & Shafiullah, G. M. Hydrogen production for energy: An overview. *Int J. Hydrog. Energy* **45**, 3847–3869 (2020).
14. Öberg, S., Odenberger, M. & Johnsson, F. The value of flexible fuel mixing in hydrogen-fueled gas turbines – A techno-economic study. *Int J. Hydrog. Energy* **47**, 31684–31702 (2022).
15. Nurdiawati, A. et al. Towards fossil-free steel: Life cycle assessment of biosyngas-based direct reduced iron (DRI) production process. *J. Clean. Prod.* **393**, 136262 (2023).
16. Guo, J. et al. Direct seawater electrolysis by adjusting the local reaction environment of a catalyst. *Nat. Energy* **8**, 264–272 (2023).
17. Li, Y. et al. Study the effect of lye flow rate, temperature, system pressure and different current density on energy consumption in catalyst test and 500W commercial alkaline water electrolysis. *Mater. Today Phys.* **22**, 100606 (2022).
18. Schmidt, O. et al. Future cost and performance of water electrolysis: An expert elicitation study. *Int J. Hydrog. Energy* **42**, 30470–30492 (2017).
19. Kraglund, M. R. et al. Ion-solvating membranes as a new approach towards high rate alkaline electrolyzers. *Energy Environ. Sci.* **12**, 3313–3318 (2019).
20. Dotan, H. et al. Decoupled hydrogen and oxygen evolution by a two-step electrochemical–chemical cycle for efficient overall water splitting. *Nat. Energy* **4**, 786–795 (2019).
21. Yang, F., Kim, M. J., Brown, M. & Wiley, B. J. Alkaline water electrolysis at 25 A cm⁻² with a microfibrous flow-through electrode. *Adv. Energy Mater.* **10**, 2001174 (2020).
22. Omrani, R. & Shabani, B. Gas diffusion layer modifications and treatments for improving the performance of proton exchange membrane fuel cells and electrolysers: A review. *Int. J. Hydrog. Energy* **42**, 28515–28536 (2017).
23. Park, J. E. et al. Effect of pore structures in nickel-based porous transport layers for high-performance and durable anion-exchange membrane water electrolysis. *Int. J. Energy Res.* **46**, 16670–16678 (2022).
24. Hu, X., Liu, M., Huang, Y., Liu, L. & Li, N. Sulfonate-functionalized polybenzimidazole as ion-solvating membrane toward high-performance alkaline water electrolysis. *J. Memb. Sci.* **663**, 121005 (2022).

25. de Groot, M. T. & Vreman, A. W. Ohmic resistance in zero gap alkaline electrolysis with a Zirfon diaphragm. *Electrochim. Acta* **369**, 137684 (2021).

26. Du, N. et al. Anion-Exchange Membrane Water Electrolyzers. *Chem. Rev.* **122**, 11830–1189513 (2022).

27. Deng, X., Yang, F., Li, Y., Dang, J. & Ouyang, M. Quantitative study on gas evolution effects under large current density in zero-gap alkaline water electrolyzers. *J. Power Sources* **555**, 232378 (2023).

28. Angulo, A. E., Frey, D. & Modestino, M. A. Understanding Bubble-Induced Overpotential Losses in Multiphase Flow Electrochemical Reactors. *Energy Fuels* **36**, 7908–7914 (2022).

29. Dukovic, J. & Tobias, C. W. The influence of attached bubbles on potential drop and current distribution at gas-evolving electrodes. *J. Electrochem. Soc.* **134**, 331 (1987).

30. Haverkort, J. W. & Rajaei, H. Voltage losses in zero-gap alkaline water electrolysis. *J. Power Sources* **497**, 229864 (2021).

31. Ju, W. et al. Lab-Scale Alkaline Water Electrolyzer for Bridging Material Fundamentals with Realistic Operation. *ACS Sustain. Chem. Eng.* **6**, 4829–4837 (2018).

32. Schalenbach, M. et al. Acidic or Alkaline? Towards a New Perspective on the Efficiency of Water Electrolysis. *J. Electrochem. Soc.* **163**, F3197 (2016).

33. Lee, H. I. et al. Advanced Zirfon-type porous separator for a high-rate alkaline electrolyser operating in a dynamic mode. *J. Memb. Sci.* **616**, 118541 (2020).

34. Lee, J. W. et al. Cellulose nanocrystals–blended zirconia/polysulfone composite separator for alkaline electrolyzer at low electrolyte contents. *Chem. Eng. J.* **428**, 131149 (2022).

35. Wang, J. Theory and practice of flow field designs for fuel cell scaling-up: A critical review. *Appl. Energy* **157**, 640–663 (2015).

36. Lin, R., Lu, Y., Xu, J., Huo, J. & Cai, X. Investigation on performance of proton exchange membrane electrolyzer with different flow field structures. *Appl. Energy* **326**, 120011 (2022).

37. Bear, J. & Bachmat, Y. *Introduction to modeling of transport phenomena in porous media*, Vol. 4 (Kluwer Academic Publishers, Dordrecht, The Netherlands, 1990).

38. Meinicke, S., Möller, C.-O., Dietrich, B., Schlüter, M. & Wetzel, T. Experimental and numerical investigation of single-phase hydrodynamics in glass sponges by means of combined μPIV measurements and CFD simulation. *Chem. Eng. Sci.* **160**, 131–143 (2017).

39. Zafari, M., Panjepour, M., Davazdah Emami, M. & Meratian, M. Microtomography-based numerical simulation of fluid flow and heat transfer in open cell metal foams. *Appl. Therm. Eng.* **80**, 347–354 (2015).

40. Ranut, P., Nobile, E. & Mancini, L. Microtomography-based CFD Analysis of Transport in Open-Cell Aluminum Metal Foams. *J. Phys. Conf. Ser.* **501**, 12021 (2014).

41. Sadeghi, M., Mirdrikvand, M., Pesch, G. R., Dreher, W. & Thöming, J. Full-field analysis of gas flow within open-cell foams: comparison of micro-computed tomography-based CFD simulations with experimental magnetic resonance flow mapping data. *Exp. Fluids* **61**, 124 (2020).

42. Kuhlmann, K. et al. From μCT data to CFD: an open-source workflow for engineering applications. *Eng. Appl. Comput. Fluid Mech.* **16**, 1706–1723 (2022).

43. Rocha, F., Delmelle, R., Georgiadis, C. & Proost, J. Effect of pore size and electrolyte flow rate on the bubble removal efficiency of 3D pure Ni foam electrodes during alkaline water electrolysis. *J. Environ. Chem. Eng.* **10**, 107648 (2022).

44. Rocha, F., Delmelle, R., Georgiadis, C. & Proost, J. Electrochemical Performance Enhancement of 3D Printed Electrodes Tailored for Enhanced Gas Evacuation during Alkaline Water Electrolysis. *Adv. Energy Mater.* **13**, 2203087 (2022).

45. Schiller, G., Henne, R. & Borck, V. Vacuum plasma spraying of high-performance electrodes for alkaline water electrolysis. *J. Therm. Spray. Technol.* **4**, 185–194 (1995).

46. He, Z. et al. Activating lattice oxygen in NiFe-based (oxy) hydroxide for water electrolysis. *Nat. Comm.* **13**, 2191 (2022).

47. Park, K. R. et al. NiFe layered double hydroxide electrocatalysts for an efficient oxygen evolution reaction. *ACS Appl. Energy Mater.* **5**, 8592–8600 (2022).

48. Vermeiren, P., Adriansens, W., Moreels, J. P. & Leysen, R. Evaluation of the Zirfon® separator for use in alkaline water electrolysis and Ni-H₂ batteries. *Int. J. Hydrog. Energy* **23**, 321–324 (1998).

49. Lohrberg, K. & Kohl, P. Preparation and use of Raney-Ni activated cathodes for large scale hydrogen production. *Electrochim. Acta* **29**, 1557–1561 (1984).

50. Kayser, A. et al. Raney-nickel cathodes from Al-Mo-Ni precursor alloys for alkaline water electrolysis. *Z. fuer Metallkd. Mater. Res. Adv. Tech.* **83**, 565–568 (1992).

51. Cardoso, D. S. P. et al. Hydrogen evolution on nanostructured Ni-Cu foams. *RSC Adv.* **5**, 43456–43461 (2015).

52. Mistry, H., Varela, A. S., Kühl, S., Strasser, P. & Cuenya, B. R. Nanostructured electrocatalysts with tunable activity and selectivity. *Nat. Rev. Mater.* **115**, 16009 (2016).

53. Li, X., Walsh, F. C. & Pletcher, D. Nickel based electrocatalysts for oxygen evolution in high current density, alkaline water electrolysers. *Phys. Chem. Chem. Phys.* **13**, 1162–1167 (2011).

54. Sakas, G. et al. Sensitivity analysis of the process conditions affecting the shunt currents and the SEC in an industrial-scale alkaline water electrolyzer plant. *Appl. Energy* **359**, 122732 (2024).

55. Jupudi, R. S., Zappi, G. & Bourgeois, R. Prediction of shunt currents in a bipolar electrolyzer stack by difference calculus. *J. Appl. Electrochem.* **37**, 921–931 (2007).

56. White, R. E., Walton, C. W., Burney, H. S. & Beaver, R. N. Predicting shunt currents in stacks of bipolar plate cells. *J. Electrochem. Soc.* **133**, 485 (1986).

57. Skas, G. et al. Influence of shunt currents in industrial-scale alkaline water electrolyzer plants. *Renew. Energy* **225**, 120266 (2024).

58. Walsh, F. C. & Ponce de León, C. Progress in electrochemical flow reactors for laboratory and pilot scale processing. *Electrochim. Acta* **280**, 121–148 (2018).

59. Arenas, L., Ponce de León, C. & Walsh, F. C. Critical review-the versatile plane parallel electrode geometry: an illustrated review. *J. Electrochem. Soc.* **167**, 023504 (2020).

60. Zhang, J. et al. Efficient hydrogen production on MoNi4 electrocatalysts with fast water dissociation kinetics. *Nat. Commun.* **8**, 15437 (2017).

61. Razmjooei, F. et al. Elucidating the Performance Limitations of Alkaline Electrolyte Membrane Electrolysis: Dominance of Anion Concentration in Membrane Electrode Assembly. *ChemElectroChem* **7**, 3951–3960 (2020).

62. Schalenbach, M. et al. Nickel-molybdenum alloy catalysts for the hydrogen evolution reaction: Activity and stability revised. *Electrochim. Acta* **259**, 1154–1161 (2018).

63. Anantharaj, S., Kundu, S. & Noda, S. Worrisome Exaggeration of Activity of Electrocatalysts Destined for Steady-State Water Electrolysis by Polarization Curves from Transient Techniques. *J. Electrochem. Soc.* **169**, 14508 (2022).

64. Edelsbrunner, H., Kirkpatrick, D. & Seidel, R. On the shape of a set of points in the plane. *IEEE Trans. Inf. Theory* **29**, 551–559 (1983).

65. Geuzaine, C. & Remacle, J.-F. Gmsh: A 3-D finite element mesh generator with built-in pre- and post-processing facilities. *Int. J. Numer Methods Eng.* **79**, 1309–1331 (2009).

66. Constant, M., Dubois, F., Lambrechts, J. & Legat, V. Implementation of an unresolved stabilised FEM–DEM model to solve immersed granular flows. *Comput. Part Mech.* **6**, 213–226 (2019).

67. Le Bideau, D., Mandin, P., Benbouzid, M., Kim, M. & Sellier, M. Review of necessary thermophysical properties and their sensivities with temperature and electrolyte mass fractions for alkaline water electrolysis multiphysics modelling. *Int. J. Hydrog. Energy* **44**, 4553–4569 (2019).

68. LeRoy, R. L., Bowen, C. T. & LeRoy, D. J. The Thermodynamics of Aqueous Water Electrolysis. *J. Electrochem. Soc.* **127**, 1954 (1980).

69. Gilliam, R. J., Graydon, J. W., Kirk, D. W. & Thorpe, S. J. A review of specific conductivities of potassium hydroxide solutions for various concentrations and temperatures. *Int. J. Hydrog. Energy* **32**, 359–364 (2007).

70. Phillips, R., Edwards, A., Rome, B., Jones, D. R. & Dunnill, C. W. Minimising the ohmic resistance of an alkaline electrolysis cell through effective cell design. *Int. J. Hydrog. Energy* **42**, 23986–23994 (2017).

71. Karacan, C. et al. Challenges and important considerations when benchmarking single-cell alkaline electrolyzers. *Int. J. Hydrog. Energy* **47**, 4294–4303 (2022).

72. Lopata, J. S. et al. Investigating influence of geometry and operating conditions on local current, concentration, and crossover in alkaline water electrolysis using computational fluid dynamics. *Electrochim. Acta* **390**, 138802 (2021).

73. Kim, S. et al. Highly selective porous separator with thin skin layer for alkaline water electrolysis. *J. Power Sources* **524**, 231059 (2022).

74. Ali, M. F. et al. Zirconia Toughened Alumina-Based Separator Membrane for Advanced Alkaline Water Electrolyzer. *Polymers* **14**, 1173 (2022).

Acknowledgements

Author contributions

F.R., R.D. and J.P. conceived the idea and designed the experiments. F.R., R.D. and X.P. built the electrochemical systems and performed the electrochemical experiments. S.M. assisted in the design and interpretation of the EIS measurements. C.G. and K.V. developed and performed the CFD simulations. G.P. performed the X-ray micro-computed tomography, and contributed with G.K. to its data analysis and interpretation. F.E. and F.R. developed and performed the Raney Ni coating process, and contributed with S.A. to its evaluation. F.R., R.D., C.G., K.V. and J.P. performed data analysis, interpretation of the results, and preparation of the manuscript. All authors contributed to reviewing and editing of the manuscript.

Competing interests

Additional information